Delta⁴
by ScandiDos

Be confident implementing Radixact Synchrony clinically

THE ONLY PLATFORM MOVING IN 7 DIMENSIONS*

We provide you with a realistic pre-treatment verification of the delivered treatment for Radixact Synchrony.

In collaboration with Accuray, ScandiDos has developed a solution that improves the quality assurance (QA) of radiotherapy treatments of moving targets. The solution independently simulates the breathing motion of patients, therefore, adding a seventh dimension to the tumor movement simulation provided by the Delta4 HexaMotion.

*longitudinal, lateral, height, roll, tilt, time and breathing motion.

Learn more ▶

Delta4family.com

Assessment of intracoronary stent location and extension in intravascular ultrasound sequences

Simone Balocco[a)]
Department of Matematics and Informatics, University of Barcelona, Gran Via 585, 08007 Barcelona, Spain
Computer Vision Center, 08193 Bellaterra, Spain

Francesco Ciompi
Department of Pathology University Medical Center, Nijmegen, The Netherlands
Diagnostic Image Analysis Group, Radboud University Medical Center, Nijmegen, The Netherlands

Juan Rigla
InspireMD, Boston, MA, USA

Xavier Carrillo and Josepa Mauri
University Hospital Germans Trias i Pujol, 08916, Badalona, Spain

Petia Radeva
Department of Matematics and Informatics, University of Barcelona, Gran Via 585, 08007 Barcelona, Spain
Computer Vision Center, 08193 Bellaterra, Spain

(Received 16 February 2018; revised 11 October 2018; accepted for publication 12 October 2018; published 14 December 2018)

Purpose: An intraluminal coronary stent is a metal scaffold deployed in a stenotic artery during percutaneous coronary intervention (PCI). In order to have an effective deployment, a stent should be optimally placed with regard to anatomical structures such as bifurcations and stenoses. Intravascular ultrasound (IVUS) is a catheter-based imaging technique generally used for PCI guiding and assessing the correct placement of the stent. A novel approach that automatically detects the boundaries and the position of the stent along the IVUS pullback is presented. Such a technique aims at optimizing the stent deployment.
Methods: The method requires the identification of the stable frames of the sequence and the reliable detection of stent struts. Using these data, a measure of likelihood for a frame to contain a stent is computed. Then, a robust binary representation of the presence of the stent in the pullback is obtained applying an iterative and multiscale quantization of the signal to symbols using the Symbolic Aggregate approXimation algorithm.
Results: The technique was extensively validated on a set of 103 IVUS of sequences of *in vivo* coronary arteries containing metallic and bioabsorbable stents acquired through an international multicentric collaboration across five clinical centers. The method was able to detect the stent position with an overall F-measure of 86.4%, a Jaccard index score of 75% and a mean distance of 2.5 mm from manually annotated stent boundaries, and in bioabsorbable stents with an overall F-measure of 88.6%, a Jaccard score of 77.7 and a mean distance of 1.5 mm from manually annotated stent boundaries. Additionally, a map indicating the distance between the lumen and the stent along the pullback is created in order to show the angular sectors of the sequence in which the malapposition is present.
Conclusions: Results obtained comparing the automatic results vs the manual annotation of two observers shows that the method approaches the interobserver variability. Similar performances are obtained on both metallic and bioabsorbable stents, showing the flexibility and robustness of the method. © *2018 American Association of Physicists in Medicine* [https://doi.org/10.1002/mp.13273]

Key words: IVUS, malapposition, stent, ultrasound

1. INTRODUCTION

An intraluminal coronary stent is a metal mesh tube deployed in a stenotic artery during percutaneous coronary intervention (PCI) in order to restore blood flow. The assessment of the stent location and extension along the vessel axis is relevant for PCI planning, implantation, and patient follow up. In order to have an effective deployment, a stent should be optimally placed with regard to anatomical structures such as bifurcations and stenoses. The deployment of a stent in an incorrect location may lead to restenosis[1] or bifurcation side branch occlusion.[2]

Although the current reference image modality for verifying the correct positioning of a stent is intravascular optical coherence tomography (OCT), a potential alternative is intravascular ultrasound (IVUS). IVUS is a catheter-based imaging technique that provides the sequence of tomographic images (pullback) of the internal vessel morphology [see Fig. 1(a)]. The stent placement can be deduced by the position of its struts, [see Fig. 1(b)].[3] The main advantage of OCT over IVUS is that the resolution is 10-fold higher, easing the visualization of the stent for the physician. However, OCT remains inferior to IVUS in matters of depth of penetration

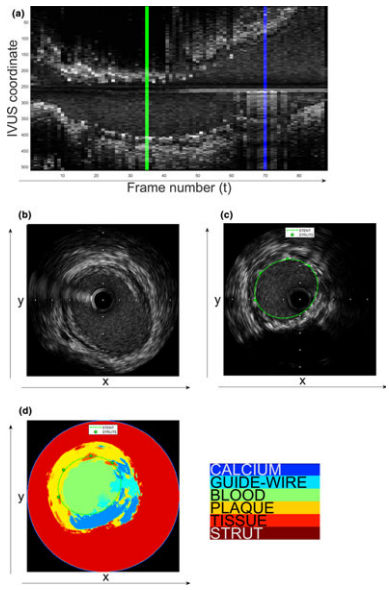

FIG. 1. Example of IVUS pullback containing a stent (a). In (b) and (c), two examples of IVUS frames in Cartesian coordinates, and belonging to the pullback (a), are depicted. The frame (b) corresponds to the green vertical line in (a), and it does not contain a stent, while (c) corresponds to the vertical line in (a), and it contains a stent. The green circles and the green dotted line in (c) and (d) represent the estimated position of struts and stent shape obtained using the technique.[3] The classification map (d) of the IVUS frame (c) is used to guide the struts and stent estimation. [Color figure can be viewed at wileyonlinelibrary.com]

(1.5 vs 5 mm),[4] which limits its ability to assess plaque burden, bifurcation angles[5], and vessel remodeling. Moreover, the guiding OCT catheter requires the intubation of the coronary ostium in order to effectively provide contrast injection, limiting the analysis of ostial and occlusive lesions. Consequently IVUS is regarded as either complementary or preferable to OCT in complex lesions.[6–8]

The IVUS images can be visualized in a long-axis view, allowing a pullback-wise analysis and in short-axis view for frame-wise analysis [see Figs. 1(a) and 1(b)]. The physician examines both views in order to perform a diagnosis of the correct stent deployment. On one hand the pullback-wise analysis allows the physician to localize the position of the stent within other vascular structures and produce a rough estimate of stent length. On the other hand, the frame-wise analysis allows a refinement of the assessment by detecting the initial and the final frame in which the stent is present, by assessing if struts appear in a frame. Some struts might not be visible in the long-axis view of the pullback because of the chosen angle for the visualization.

To date, several approaches allowing the detection and 3D reconstruction of stents from OCT images have been published,[9–11] since the high image resolution allows a detailed identification of the struts along the pullback. Instead, in IVUS the visualization and rendering of the 3D shape of the stent is feasible,[12,13] but the accurate strut detection and the longitudinal localization of the stent along the pullback remains a challenging task.[14,15] In IVUS images, only a few struts are often visible, due to the inclination of the ultrasonic probe with regard to the longitudinal axis of the vessel. Several regions in the IVUS image may look similar to a strut, due to their local appearance (guide-wire artifacts, refractions of ultrasonic waves, reverberations or presence of small calcifications or dense fibrotic tissue in contact with the stent) as illustrated in Figs. 1(b) and 1(c)]. Additionally, the strut texture and the thickness may vary depending on the type of implanted stent, which can be either metallic or bioabsorbable.[16,17] As a consequence, the analysis of a single short-axis image may not be sufficient for accurately assessing if struts are present. In most of ambiguous cases, the physician has to scroll the pullback back and forward, analyzing adjacent frames in order to identify the frames defining the stent boundaries.

Few approaches for automatic stent analysis in IVUS have been proposed so far.[3,18–22] All the existing methods aim at identifying the struts in the short-axis view of the pullback assuming that the analyzed frame always contains a stent; these methods therefore rely on the presence of struts in the axial frame. Indeed, so far no strategies have been proposed for detecting if the stent is present in the frame, and for finding the boundaries and the position of the stent along the pullback. A possible reason could be that in most of the published techniques,[3,18–22] the number of false positive strut were too high, making difficult to differentiate a frame containing a stent (a stent frame) from others in an IVUS pullback. Instead, this paper extends a strut detection method for metallic and bioabsorbable stent that results more robust that previous stent detection approaches,[3] and using the struts detection obtained in successive short-axis views, estimates the location and extension of the stent along the pullback.

1.A. Our contribution

A novel approach that automatically detects the boundaries and the position of the stent along the IVUS pullback is presented. The pipeline of the method consists of three steps: (1) the identification of the stable frames of the sequence, (2) the detection of stent struts, and (3) the assessment of the stent presence (location and extension) along the pullback. In this paper, an image-based gating technique[23] and a struts detection method[3] were used to obtain (1) and (2), considering the superior performance of such methods with regard to other state of the art options, while a novel approach has been designed for (3). In particular, phase (3) consists of defining a measure of likelihood for a frame to contain a stent, which we call *stent presence*. A temporal series is obtained by computing such a likelihood along the whole sequence. The mono-dimensional signal is modeled as a train of rectangular waves by using an iterative and multiscale approximation of the signal to symbols using the SAX (Symbolic Aggregate approXimation) algorithm,[27] which was initially introduced as low computational complexity method for classic data mining tasks such as clustering, classification, and indexing. In this paper, SAX is used for the first time to obtain an unsupervised and robust binary representation of the signal representing the *stent presence* in a pullback.

The coupling of new strategy for the assessment of stent location and extension of intracoronary stent with the previous published methods[3,23] provides a complete framework for detection of intracoronary stents aimed at assisting intraoperative diagnosis.

Instead, to the best of our knowledge, it is the first time that a strategy for assessing the stent presence has been presented. Preliminary results of our approach on a reduced image dataset was presented in Ref. [24]. This paper extends[24] by focusing on an extensive validation using a set of 103 IVUS sequences of *in vivo* coronary arteries containing metallic and bioabsorbable stents, which are acquired through an international multicentric collaboration across five centers. Precision, Recall, F-measure, and Jaccard scores along with the distance between detected and reference frames are reported, and compared against inter- and intraobserver measurements of two experts.

Additionally, applying the framework to each IVUS-gated frame allows to estimate the lumen and stent contours. Using such information it is possible to compute the stent malapposition for each angular sector of the frame along the pullback. As a result, a map indicating the distance between the lumen and the stent in each angular section of the pullback is created and the angular sector of the pullback displaying malapposition is identified.

2. MATERIALS AND METHOD

The three steps of the framework are detailed in the following sections.

2.A. Gating

Let us define an IVUS pullback as a sequence of frames $I = \{f_i\}$ where i is the frame number of the sequence. We first preprocess the pullback by applying an image-based gating procedure. Gating allows to reduce the *swinging* and *roto-pulsation* effects[3] affecting the reliable identification of luminal area,[25] which is an important factor for the strut detection.[26] In our pipeline, a sequence of gated frames $G = \{f_{g_j}\}$ is obtained by applying the method presented by Gatta et al.[23] to the IVUS pullback. It is worth noting that $G \subset I$ and that each index $g_j \approx 35i$, assumes a heart rate of approximately 60–80 bpm.

2.B. Strut detection

The detection of stent struts was performed by applying the strut detection method proposed by Ciompi et al.[3] to each gated frame independently. The method identifies the stent struts by contemporaneously considering the textural appearance of the stent and the vessel morphology. The strut detection system uses the Multi-Scale Multi-Class Stacked Sequential Learning (M^2SSL) classification scheme to provide a comprehensive interpretation of the local structure of the vessel. In the classification problem, the class *Strut* is considered as one of the six considered classes (defined as Blood area, Plaque, Calcium, Guide-wire shadow, Strut, and external Tissues). For semantic classification purposes, tailored features used for classification to the problem[26] are used.

As a result, for each pixel $p(x,y)$ of a gated IVUS image, a classification map M is obtained [see Fig. 1(d)]. A curve approximating the stent shape S_{shape} is initially estimated considering vascular constrains and classification results. For each region of M labeled as stent $(M_{\{S\}})$, a strut candidate is considered. The selected struts $p_s(x, y)$ were selected among the candidates, considering both local *appearance* and distance with regard to the stent shape S_{shape}. Consequently false-positive candidates were discarded, and the regions containing a selected strut $M^*_{\{S\}}$ are a subset of $M_{\{S\}}$.

2.C. Stent presence assessment

The frames of the pullback corresponding to the vessel positions where the stent begins and ends can be identified by analyzing the detected struts. We model the presence of stent as a rectangular function $\sqcap(t)$, where the variable t indicates the temporal position in the pullback (see Fig. 1). We estimate the binary signal $\sqcap(t)$ by processing a real-valued signal $\gamma(t)$, which we define *stent presence*, corresponding to the frame-based likelihood of finding a stent in each frame of the IVUS sequence. The value of $\gamma(t)$ for each position t in the sequence is computed by considering both the number of struts and their area, thus negatively weighting small strut areas of the images which have an high probability to be incorrect detections.

$$\gamma(t) = \sum_{p \in M^*_{\{S\}}} p|_{p_s \in M^*_{\{S\}}} \tag{1}$$

where $p_s \in M^*_{\{S\}}$ indicates the pixels of the IVUS frame labeled as *strut* containing an selected strut. An example of signal $\gamma(t)$ is depicted in Fig. 2(c).

The signal $\gamma(t)$ may contain several transitions between low and high amplitudes, due to the variability in the number of struts visible in consecutive frames and to suboptimal strut detection. For this reason, we filter the $\gamma(t)$ signal by considering its local statistics applying the SAX algorithm.[27] SAX is a symbolic representation algorithm that estimates a quantization of the time series based on global signal measurements and on local statistics of subsequent neighbor samples. Given the signal $\gamma(t)$ and a window size w, the algorithm calculates a Piecewise Aggregate Approximation (PAA) $\widehat{\gamma(t)}$, which is obtained by computing the local average values of $\gamma(t)$ over n_w segments w-wide. Each average value is then normalized over the signal $\underline{\gamma(t)}$. The procedure firstly computes a vector $\overline{\gamma(t)} = (\overline{q}_1, \ldots, \overline{q}_{n_w})$ where each of $\overline{q}_i$ is calculated as follows:

$$\overline{q}_i = \frac{1}{w} \sum_{j=w(i-1)+1}^{w \cdot i} q_j, \tag{2}$$

where $i,j \in \mathbb{N}$. The quantified signal amplitudes $\widehat{q}_i$ are obtained by normalizing $\overline{q}_i$ by the mean μ_γ and standard deviation σ_γ of the signal $\gamma(t)$:

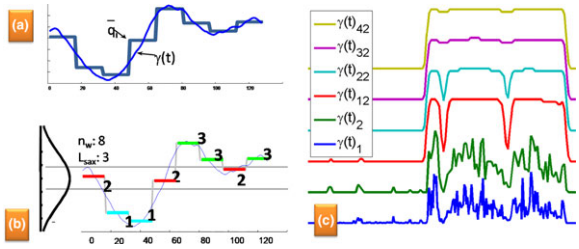

FIG. 2. In order to illustrate with an example the procedure of SAX algorithm, a Piecewise Aggregate Approximation of a synthetic curve, not related with any measurement, is depicted in (a) and (b). The method firstly computes the local average values $\overline{q}_i$ of the signal $\gamma(t)$ over n_w segment (a). Then, the algorithm normalizes the samples by the mean and standard deviation of the signal obtaining the amplitudes $\hat{q}_i$. Considering a Gaussian distribution of the samples' amplitudes, the samples $\hat{q}_i$ are mapped to L_{sax} discrete values having equi-probability (b), that is, the cutoff values are chosen in such way to separate the area below the Gaussian curve in L_{sax} equal regions. In the example of (a) and (b), the signal is quantized using $n_w = 8$ and $L_{sax} = 3$. Then, in another example (c), the SAX algorithm is applied to a signal $\gamma(t)$ obtained from an IVUS pullback. In this case, the signal $\gamma(t)$ is quantized using $n_w = 2$ and $L_{sax} = 2$. The SAX algorithm is iterated N_{sax} times over an exemplar signal $\gamma(t)_i$, where i s the iteration number. In this second case (c), the signals $\gamma(t)_i$ obtained in 6 of the 50 iterations (namely $i = 1, 2, 12, 22, 32, 42$) are illustrated. [Color figure can be viewed at wileyonlinelibrary.com]

$$\widehat{q}_i = \frac{\overline{q}_i - \mu_\gamma}{\sigma_\gamma} \tag{3}$$

Then, the $\widehat{q}_i$ amplitudes are mapped to L_{sax} discrete values. Considering a Gaussian distribution of the samples amplitudes, each value L_{sax} corresponds to an equal-sized area of the Gaussian curve.

The SAX algorithm is iterated N_{sax} times, until converging to flat intervals along the signal $\gamma(t)$. The maximum iteration number N_{sax} is achieved when the difference between subsequent iterations of SAX is zero. Figure 2(c) illustrates the iteration of the SAX algorithm over an exemplar signal $\gamma(t)$. The other parameters of the SAX algorithm is the number of quantized values assigned to the signal L_{sax}. The iterative SAX algorithm is described by the following equation:

$$\gamma(t)_{k+1} = SAX\left(\gamma(t)_k, \sigma_k^{train_{sax}}, \mu_k^{train_{sax}}, L^{train_{sax}}\right) \tag{4}$$

where $k \in 1...N_{sax}$ and $\sigma_k^{train_{sax}}$ and $\mu_k^{train_{sax}}$ are the mean and standard deviation computed on the training set at the iteration k, and the number of quantized values L_{sax} is a constant that has been optimized by cross-validation using the training set, as described in the validation section. When the SAX algorithm reaches the maximum iteration number N_{sax}, the binary signal indicating the stent presence of the stent is obtained as $\sqcap(t) = \gamma(t)_{N_{sax}} > \mu_{N_{sax}}^{train_{sax}}$.

3. VALIDATION

3.A. Material

A set of 103 sequences of IVUS images was collected through a multicenter study (see Table I). In this study, we are interested in assessing the performance of the method at detecting the presence of stent along the pullback. For this reason, pullbacks acquired before and after stent deployment were used, therefore considering also sequences with the absence of stent. The dataset includes nine pullbacks acquired before the stent deployment. The remaining 94 pullbacks contain one or more *metallic* (*met*) or *bioabsorbable* (*abs*) stents.

Data acquisition protocol was approved by the IRB of each clinical centre. The IVUS sequences were acquired using iLab echograph (Boston Scientific, Fremont, CA) with a 40 MHz catheter (Atlantis SR Pro, Boston Scientific); no standardization of the echograph parameters was applied during the acquisitions. The pullback speed was 0.5 mm/s and the IVUS system had a 30 frames per second frame rate. The model of the metallic and bioabsorbable stents were "Promus Coronary Stent, Boston Scientific, MN" and "Absorb Bioresorbable Vascular Scaffold (BVS), Abbott, IL", respectively.

Two experts (one clinician and one experienced researcher in IVUS imaging) manually annotated the beginning and the end of the stent in each sequence. They were asked to scroll the pullback back and forward, looking at the short-axis view only, and analyzing adjacent frames in order to identify the frames defining the stent boundaries. More than one annotation per pullback was allowed when several stents were implanted in subsequent segments of the same artery. Two separate test sets were defined ($test_{met}$ and $test_{abs}$), corresponding to pullback containing metallic or bioabsorbable stents, respectively. When sequences containing a metallic stent were tested the training was performed using pullbacks having a metallic stent ($train_{met}$). Instead when sequences containing bioabsorbable stent were analyzed, the training was performed separately using metallic ($train_{met}$) or bioabsorbable ($train_{abs}$) frames. Since the number of sequences containing a bioabsorbable stent was low, we expect that the stent detection performance might increase when the system is trained on a larger dataset. When pullbacks of the same dataset were used for test and training, a 10-fold cross-validation strategy was used to compute the results, while all the metallic pullbacks ($train_{met}$) were used for training purposes when the test was performed over $test_{abs}$ dataset.

3.B. Experiments on stent presence assessment

The assessment of stent presence is based on the analysis of the mono-dimensional signal $\gamma(t)$. In order to evaluate the performance, the manual annotations of the beginning and end of the stent were converted into binary signals $\gamma_{obs}(t)$ indicating the presence of the stent in the pullback. Successively, the signals $\sqcap(t)$ indicating the segments of the pullback in which a stent is likely to be present, were compared against the sections indicated by the observers $\gamma_{obs}(t)$. The performance was evaluated by measuring the *Precision (P)*, *Recall (R)*, *F-Measure (F)*, and *Jaccard-index (J)*. The first three indices are typically used to evaluate a detection problem, while the forth index evaluates the overlap between the ground-truth and the automatically detected signals. Additionally, the distance between the automatic and the manual detection expressed as the number of gated frames, in *mm*, and as percentage of the stent length.

TABLE I. Detailed description of the datasets used in this study.

Dataset type	Hospital	Number of pullbacks	Stent deployment	% of stent frames	Training	Test
Metallic	#1	80	Deployed	Roughly 50%	$train_{met}$	$test_{met}$
	#2	3	Deployed	Roughly 50%	$train_{met}$	$test_{met}$
		1	Predeployed	0%	$train_{met}$	$test_{met}$
	#3	5	Deployed	Roughly 50%	$train_{met}$	$test_{met}$
		3	Predeployed	0%	$train_{met}$	$test_{met}$
Bioabsorbable		1	Deployed	Roughly 50%	$train_{met}/train_{abs}$	$test_{abs}$
		1	Predeployed	0%	$train_{met}/train_{abs}$	$test_{abs}$
	#4	4	Deployed	Roughly 50%	$train_{met}/train_{abs}$	$test_{abs}$
		3	Predeployed	0%	$train_{met}/train_{abs}$	$test_{abs}$
	#5	1	Deployed	Roughly 50%	$train_{met}/train_{abs}$	$test_{abs}$
		1	Predeployed	0%	$train_{met}/train_{abs}$	$test_{abs}$

In our experiments, we estimate $\sigma_k^{train_{sax}}$, $\mu_k^{train_{sax}}$ and $L^{train_{sax}}$ by optimizing the F-measure score by varying L_{sax} between 3 and 50. When the optimal value of $L_{sax} = 36$ is set, $\sigma_k^{train_{sax}}$, $\mu_k^{train_{sax}}$ are estimated automatically by the SAX algorithm.

The quantitative results for the pullback-wise analysis for the three experiments are reported in Table II. In the first experiment, the system is trained and tested using metallic pullbacks. In the second and the third, the test is performed over bioabsorbable frames, and the training is obtained using metallic and bioabsorbable data, respectively. As IVUS is highly challenging to interpret, the two observers sometimes disagree as shown in Table II (rows 5, 8, and 11).

In the case of bioabsorbable stents, the best performances are obtained when the framework is trained using metallic frames. All the performance metrics (excepts the Precision) of the second experiment, that is, training using metallic frames (rows 6, 7), are higher with respect to the results obtained in the third experiment, that is, training using bioabsorbable frames (rows 9, 10). In particular, a 10% of difference between the Recall and Jaccard measure of the two experiments can be noticed. This confirms that the bioabsorbable dataset is too small for training purposes.

If we focus on the first two experiments (rows 3–8), in both datasets, the precision approaches the interobserver variability, while the recall is in general between 10% and 20% lower than the results of the manual annotation. The obtained F-measure and the Jaccard measure of the automatic performance show satisfactory results when compared with manual annotations (about 5% and 7% lower than the ground truth score).

Such results are confirmed by analyzing the distance between the boundary assessed with our method and the manual annotations, as illustrated in the last two columns of Table II. In the case of metallic stents, the error in the boundary assessment ranges between 4 and 5.3 gated frames (about 2 and 2.5 mm, respectively). It is interesting to note that such errors correspond in average to 4.2% and 5.8% of the stent length. In the case of metallic stents, the error in the boundary assessment is about 3.4 gated frames (about 1.5 mm). In this case, such an error corresponds in average to 10% of the stent length, given that the length of the bioabsorbable stents composing our dataset was in general smaller than the metallic ones. The results shown in Table II illustrate that the method is flexible and can be applied to a pullback containing either metallic or bioabsorbable stents with similar results.

In order to analyze if the scores obtained by the automatic method were statistically different from the performance of the manual annotation, an ANOVA test was performed over the results reported in Table II. As can be observed in Table III, the performances of the method were particularly satisfying, since in the case of metallic stent the automatic method approaches the performances of one observer. The error of boundary detection committed by the automatic method was found to be comparable with respect to the errors committed by the first observer, and the difference of F-measure and Jaccard scores committed by the automatic method with respect to the manual annotation, was statistically weak ($0.01 < P < 0.05$). On the other hand, the results were found to be statistically different ($P < 0.01$) when the automatic method was compared against the manual annotation of the second observer.

In the case of bioabsorbable frames trained using metallic pullbacks, comparable results were found only in the relative boundary errors, while in the other cases the results

TABLE II. Quantitative evaluation the pullback analysis stage on both $test_{met}$ and $test_{abs}$ datasets. For each dataset, the performance of the automatic method vs each manual annotation is reported. Then the interobserver variability is shown. For each experiment, the Precision, Recall, F-Measure, and Jaccard index are reported, along with the error in the boundary assessment, expressed in number of gated frames, and in percentage of the stent length.

		Precision Mean (SD)	Recall Mean (SD)	F-measure Mean (SD)	Jaccard Mean (SD)	Boundary err.(gatedfr.) Mean (SD)	Boundary err., relative Mean (SD)
$test_{met}/train_{met}$	*auto* vs *obs-1*	91.0% (15.8%)	87.4% (14.5%)	87.5% (12.0%)	79.6% (17.6%)	4.0 (5.6)	4.2% (3.8%)
	auto vs *obs-2*	94.3% (12.2%)	79.3% (16.4%)	84.6% (11.9%)	75.0% (16.9%)	5.3 (6.0)	5.8% (4.4%)
	obs-1 vs *obs-2*	96.8% (14.1%)	99.3% (5.4%)	92.1% (10.5%)	86.7% (14.5%)	3.2 (5.0)	3.9% (2.2%)
$test_{abs}/train_{met}$	*auto* vs *obs-1*	91.8% (12.8%)	86.9% (13.4%)	88.6% (11.1%)	77.7% (13.7%)	3.4 (4.8)	10.4% (5.2%)
	auto vs *obs-2*	91.8% (12.5%)	87.4% (12.7%)	88.9% (10.4%)	78.1% (12.8%)	3.3 (4.9)	10.3% (5.7%)
	obs-1 vs *obs-2*	99.5% (1.8%)	99.0% (1.9%)	99.2% (1.2%)	98.5% (2.4%)	2.9 (6.2)	8.4% (7.4%)
$test_{abs}/train_{abs}$	*auto* vs *obs-1*	97.0% (9.0%)	75.6% (22.9%)	83.4% (16.5%)	64.3% (15.6%)	5.5 (7.5)	17.8% (7.0%)
	auto vs *obs-2*	97.4% (7.7%)	76.3% (22.9%)	84.0% (16.2%)	65.1% (15.9%)	5.3 (7.2)	16.9% (7.0%)
	obs-1 vs *obs-2*	99.5% (1.8%)	99.0% (1.9%)	99.2% (1.2%)	98.5% (2.4%)	2.9 (6.2)	8.4% (7.4%)

TABLE III. ANOVA statistical analysis of the results reported in Table 2, indicating when the performances of the automatic stent detection are significantly different with respect to the manual annotations. A *strong* or *weak statistical difference* between the results is considered when the $P < 0.01$ or between $0.01 < P < 0.05$, respectively. Otherwise, when the $P > 0.05$, the null hypothesis of statistical difference between the results cannot be rejected, hence indicating that the two performances can be considered *comparable*. The second column indicated which performances of Table 2 are considered in the ANOVA analysis.

		Precision Mean (SD)	Recall Mean (SD)	F-measure Mean (SD)	Jaccard Mean (SD)	Boundary err. (gatedfr.) Mean (SD)	Boundary err., relative Mean (SD)
$\frac{test_{met}}{train_{met}}$	$\frac{(auto\ \text{VS}\ obs-1)}{(obs-1\text{VS}\ obs-2)}$	$P < 0.01$	$P > 0.05$	$0.01 < P < 0.05$	$0.01 < P < 0.05$	$P > 0.05$	$P > 0.05$
	$\frac{(auto\ \text{VS}\ obs-2)}{(obs-1\text{VS}\ obs-2)}$	$P < 0.01$	$P < 0.01$	$P < 0.01$	$P < 0.01$	$P < 0.01$	$P > 0.05$
$\frac{test_{abs}}{train_{met}}$	$\frac{(auto\ \text{VS}\ obs-1)}{(obs-1\text{VS}\ obs-2)}$	$P < 0.01$	$0.01 < P < 0.05$	$P < 0.01$	$P < 0.01$	$P < 0.01$	$P > 0.05$
	$\frac{(auto\ \text{VS}\ obs-2)}{(obs-1\text{VS}\ obs-2)}$	$P < 0.01$	$0.01 < P < 0.05$	$P < 0.01$	$P < 0.01$	$P < 0.01$	$P > 0.05$
$\frac{test_{abs}}{train_{abs}}$	$\frac{(auto\ \text{VS}\ obs-1)}{obs-1\ \text{VS}\ obs-2)}$	$P < 0.01$	$P < 0.01$	$P < 0.01$	$P < 0.01$	$P < 0.01$	$P < 0.01$
	$\frac{(auto\ \text{VS}\ obs-2)}{(obs-1\ \text{VS}\ obs-2)}$	$P < 0.01$	$P < 0.01$	$P < 0.01$	$P < 0.01$	$P < 0.01$	$P < 0.01$

between automatic and manual detection was considered statistically different. Finally, in the case of bioabsorbable frames trained using bioabsorbable pullbacks, all the tests reported a statistical difference between the automatic and the manual detection.

3.C. Malapposition analysis

Malapposition happens when at least one stent strut is separated from the intimal surface of the arterial wall and it is generally computed as the distance between the malapposed struts and the vessel wall, and the area is measured.

In particular, the thresholds of malapposed struts depends on the stent type and brand[28] ranging from 100 μm to 160 μm. In the case of the Boston Scientific brand, we consider the stent malapposed when the distance to the lumen is higher than 130 μm. The frame-wise analysis obtained by applying the framework to each IVUS-gated frame allows to estimate the lumen and stent contours. Using such information, it is possible to compute the stent malapposition for each angular sector of the frame along the pullback. As can be seen in Fig. 3 (top) an exemplar IVUS pullback is analyzed. The framework provides a map indicating the distance between the lumen and the stent in each angular section of the pullback. Then a plot, as shown in Fig. 3 (middle), illustrates the maximum amplitude of the distance along the pullback. Finally, a third plot indicates the percentage of the stent displaying malapposition 4 (bottom).

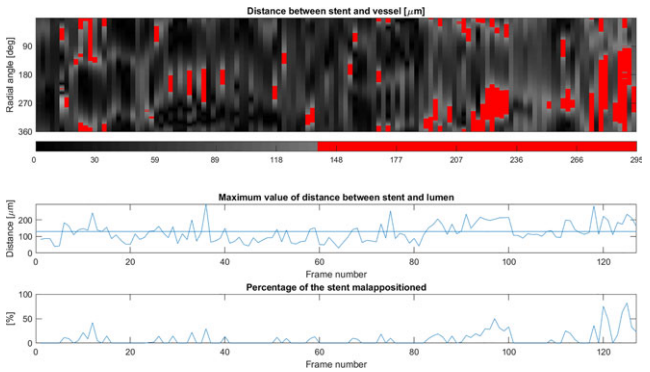

FIG. 3. Malapposition analysis of an IVUS pullback. The top image represents a distance map between the stent and the lumen. The vertical axis represents the angular section of the IVUS image, while the horizontal axis displays the position of the frame. The intensity of the map corresponds to the distance in μm. When the distance is superior to the malapposition threshold, a red color is displayed. The second plot displays the maximum amplitude of the distance between stent and lumen, along the frames of the pullback; a horizontal line indicates the malapposition threshold. The third plot displays the percentage of the stent malapposed in each frame of the pullback. [Color figure can be viewed at wileyonlinelibrary.com]

4. RESULTS

4.A. Metallic stents

Examples of processed signals for the detection of a metallic stent in the IVUS frame are depicted in Fig. 4. In Figs. 4(a1) and 4(b1), both the initial and final frame of the sequence are accurately identified. The result is not obvious since in (a) the amplitude of the signal $\gamma(t)$ is almost null in two sections of the pullback. However, the SAX algorithm allowed to detect the presence of a stent, based on the statistics of the frames in the neighborhood. On the other hand, in Fig. 4(a2), the central section of the pullback where $\gamma_{auto}(t)$ is almost null is correctly classified by the SAX algorithm as the absence of stent. This is coherent with the manual annotation of the two observers, where two stents are labeled. It must be noted that in this paper no constrain on the minimum length of the stent is applied. In 4(b2), we observed a case in which the absence of the stent is correctly identified. Indeed, observing 4(b2), it can be noticed that the quantification of the signal is below the global threshold $\mu_{N_{sax}}^{train_{pull}}$. In Figs. 4(a3) and 4(b3), regions of high signal separated from the main stent have been identified as a secondary implanted stent. It might be noticed that this error happens only when a strong spike in the signal is present, for instance when a calcified plaque is mistaken for a deployed stent. In Figs. 4 (a4) and 4(b4), the initial and final frame of the stent are incorrectly identified since the amplitude of $\gamma(t)$ is low and comparable with the noise at the proximity of the stent area.

4.B. Bioabsorbable stents

Examples of processed signals for the detection of a bioabsorbable stent in the IVUS frame are depicted in Fig. 5. In Figs. 5(a1) and 5(b1), we observe two cases of accurate stent detection. In the rest of cases the performance of the stent detection decreases. In Figs. 5(a2), 5(b2), 5(a3), the main stent was accurately detected, however one or more small peaks in the signal, having high magnitude, are incorrectly classified. In Fig. 5(a3), it is interesting to note how the algorithm is able to recover the whole stent longitude at the right side of the image, even if the signal amplitude is low at the middle of the stent area. Finally, Figs. 5(b3), 5(a4), 5(b4) show a pullback not containing a stent in which short but intense peaks in the signal are misclassified.

5. DISCUSSION

In this paper, for the first time, a framework for the automatic identification of stent presence along the pullback (location and extension) has been presented.

The methodology described in the paper is based on three main steps (1) a gating technique and (2) a stent strut detection technique used to obtain a measure of likelihood for a frame to contain a stent. The paper introduces (3) a new strategy for obtaining a robust binary representation of the presence of the stent in the pullback using the SAX algorithm. The stages (1) and (2) of the pipeline, can be computed using similar method proposed in the state of the art.[3,18–22] However, since the reliability of the strut detection is a critical step of the pipeline, the influence of using a method less reliable might have a negative impact over the performances of the whole framework.

In clinical practice, the presented system could be used intraoperatively to perform automatic analysis of the stent position and placement. This would ease the task of physicians, by reducing the burden of manual search and measurements of the deployed stent via inspection of the IVUS sequence. In order to show how the result can be represented in a clinical application, in Fig. 6, two exemplar IVUS long-axis views of the stent detection are depicted, superimposed with vertical lines representing the boundaries of the stent manually labeled by the physician.

The presented framework processes a sequence of gated frames. Due to the catheter swinging effect, nongated frames might be analyzed multiple times along the sequence. Applying gating has the advantage of providing frames that are less affected by motion artifacts, in which the analysis of blood texture can be done in a more robust and reproducible way. Moreover, gating reduces the amount of frames to be analyzed by approximately a factor 30, which also benefits the system in terms of computation time. Using gated frames does not limit the applicability of the proposed system, which can potentially work on nongated frames as well. However, in this case a reduction in performance can be expected.

The analysis of the *stent presence* signal has been performed using the SAX algorithm which provides an unsupervised classification of the stent location in a fast and statistically robust fashion.

Since the proposed system is meant to be used in an intraoperative fashion, it is important to evaluate the computational cost in order to assess its real impact during clinical practice. For this purpose, we evaluated the computation time of the system. The method has been implemented in Matlab (The MathWorks, Natick, MA, USA, 2011) and the computation time of the pullback analysis is one order of magnitude lower than the time required for detecting the stents.[3] Indeed the pullback-wise analysis took about 4.1 s per pullback vs 0.33 s per frame (around 33 s per pullback) required for a stent detection (measured on a Intel i7 quad-core processor).

6. CONCLUSION

We presented a new strategy for the assessment of stent location and extension of intracoronary stent in intravascular ultrasound sequences. Such a technique, when coupled with previous published methods,[3,23] provides a complete framework for the intracoronary stents aimed at assisting intraoperative diagnosis. The results obtained from a heterogeneous dataset, containing both metallic and bioabsorbable stents collected through a multicentric collaboration, are close to the interobserver variability and suggest that the system has the potential to be used during percutaneous interventions.

In the case of metallic stent, the performances have an overall F-measure of 87.4% and 86.4% and a Jaccard score of 76.6% and 75.0% obtained by comparing the automatic results against the manually annotated struts of the two observers, respectively. For bioabsorbable stents, the overall F-measure of 88.6%, and 88.9% was obtained, with a Jaccard score of 77.7% and 78.1% obtained by comparing the automatic results against the manually annotated struts. Such values approached the interobserver variability which corresponded to a F-measure of 92.1% and a Jaccard score of 86.7% in the case of metallic stents, and a F-measure of 99.2% and a Jaccard score of 98.5% in the case of bioabsorbable stents.

With regard to the distance between the automatic and the manual detection, the error in case of metallic stents is of 4.0 and 5.3 gated frames (corresponding to about 2 and 2.5 mm, respectively) from the manually annotated struts of the two observers, while in case of bioabsorbable stents the error is 3.4 and 3.3 gated frames (corresponding to about 1.5 mm). These results are satisfying considering that the interobserver error of the manual annotation is 3.2 and 2.9 gated frames, in case of metallic and bioabsorbable stents, respectively.

The system has been validated using cases of both metallic and bioabsorbable stents. The performances of the system were evaluated when metallic or bioabsorbable stents were used for training, and the best performances were obtained using data from cases with metallic stents, since dataset was larger. Bioabsorbable stents are used less often during PCIs, therefore finding a large set of examples was hard. However, good performance can be observed also in the presence of bioabsorbable stents, showing the capability of the system to generalize well to the detection of unseen examples, including other types of stents.

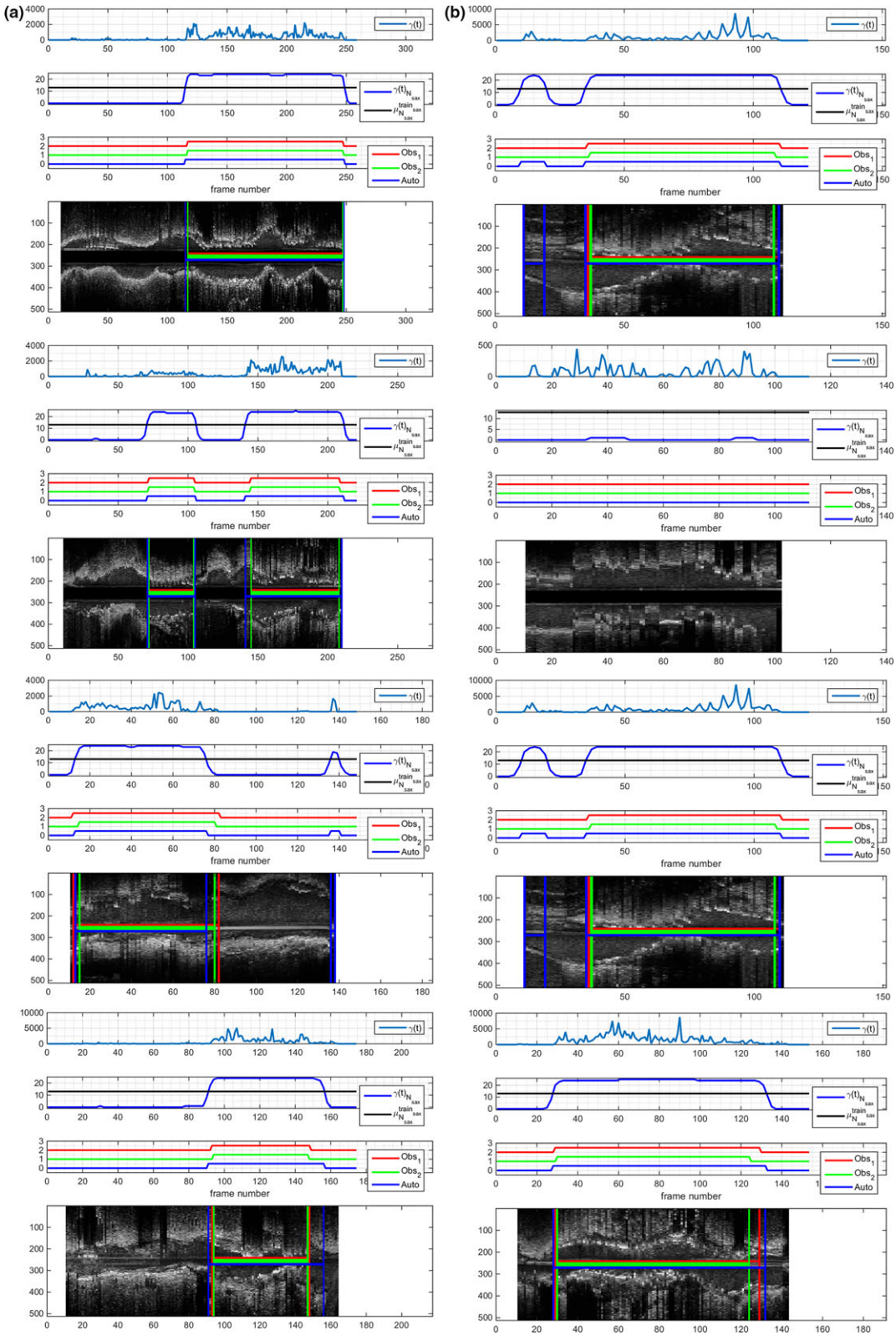

FIG. 4. Qualitative evaluation on $test_{met}$. The signal $\gamma(t)$ is illustrated in the first row, while in the second the result of the SAX quantization is reported. Finally in the third row, three binary signals representing the presence or the absence of the signal are compared: the first corresponds to the automatic results, while the second and the third are the annotations of the two observers. [Color figure can be viewed at wileyonlinelibrary.com]

Future work will be addressed toward comparing the performance of the current pipeline against the assessment of stent location and extension obtained using deep learning (DL) techniques. In particular, artificial neural networks (ANN) might improve the classification on both frame-wise and pullback-wise analyses. ANNs are well known for

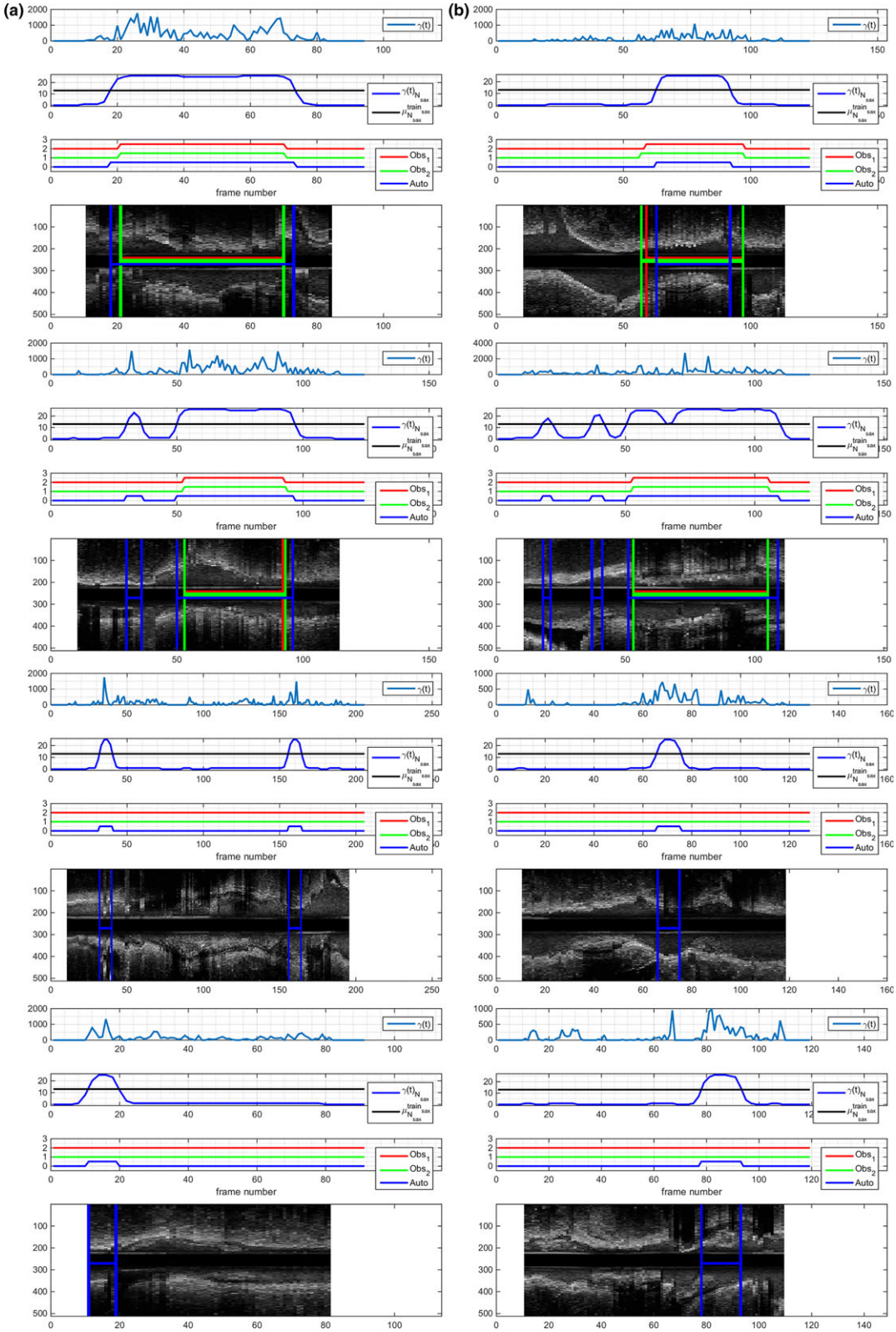

FIG. 5. Qualitative evaluation on $test_{abs}$ dataset. The signal $\gamma(t)$ is illustrated in the first row, while in the second, the result of the SAX quantization is reported. Finally in the third row, three binary signals representing the presence or the absence of the signal are compared: the first corresponds to the automatic results, while the second and the third are the annotations of the two observers. [Color figure can be viewed at wileyonlinelibrary.com]

providing state-of-the-art classification performances, however, it should be noted that ANN are currently affected by some limitations: (a) a large dataset (of the order of 10000 samples) is usually required for training purposes. (b) in literature there is not a clear consensus about how to find the optimal parameter for the network fine-tuning. Such limitations

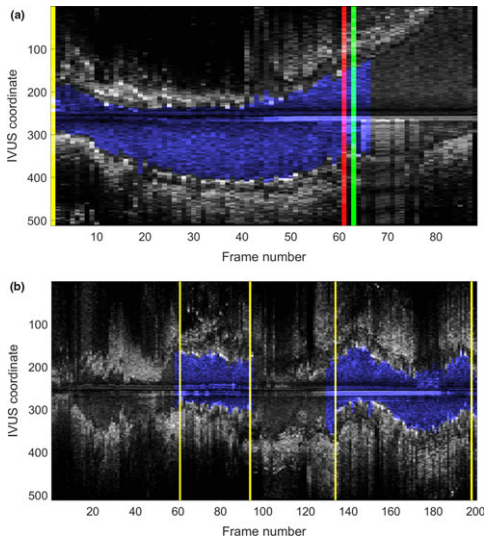

FIG. 6. Two exemplar IVUS long-axis views (a, b) of the stent detection are depicted, superimposed with red and yellow vertical lines representing the boundaries of the stent manually labelled by the experts. The *stent presence* $\Gamma(t)$ automatically computed using the SAX algorithm was indicated in blue and, for each frame, only the stent area computed by the automatic method[3] was colored. The pictures illustrate how the results can be represented in a clinical application. [Color figure can be viewed at wileyonlinelibrary.com]

should be carefully studied in order to analyze if a deep learning strategy could be successfully applied to IVUS pullbacks.

ACKNOWLEDGMENT

The authors thank Darren Barlow for the English proofread. This work was supported in part by the MICINN Grant TIN2015-66951-C2-1-R, SGR 1219, CERCA, and ICREA Academia 2014. The authors have no relevant conflicts of interest to disclose.

[a)]Author to whom correspondence should be addressed. Electronic mail: balocco.simone@gmail.com.

REFERENCES

1. Trabattoni D, Bartorelli AL. Ivus in bifurcation stenting: what have we learned?. *EuroIntervention*. 2010;6:J88–J93.
2. de Lezo JS, Medina A, Martín P, Novoa J, Pan M, Caballero E. Predictors of ostial side branch damage during provisional stenting of coronary bifurcation lesions not involving the side branch origin: an ultrasonographic study. *EuroIntervention*. 2012;7:1147–1154.
3. Ciompi F, Balocco S, Rigla J, Carrillo X, Mauri J, Radeva P. Computer-aided detection of intracoronary stent in intravascular ultrasound sequences. *Med Phys*. 2016;4:5616–5625.
4. Andell P, Karlsson S, Mohammad MA, et al. Intravascular ultrasound guidance is associated with better outcome in patients undergoing unprotected left main coronary artery stenting compared with angiography guidance alone. *Circulation*. 2017;10:e004813.
5. Alberti M, Balocco S, Gatta C, et al. Automatic bifurcation detection in coronary ivus sequences. *IEEE Trans Biomed Eng*. 2012;59:1022–2031.
6. Waggoner J. How do OCT and IVUS differ? A comparison and assessment of these modern imaging modalities. *Card Interv Today*. 2011;46–52.
7. Reiber JH, Tu S, Tuinenburg JC, Koning G, Janssen JP, Dijkstra J. QCA, IVUS and OCT in interventional cardiology in 2011. *Cardiovasc Diagn Ther*. 2011;1:57–70.
8. Waksman R, Kitabata H, Prati F, Albertucci M, Mintz GS. Intravascular ultrasound versus optical coherence tomography guidance. *J Am Coll Cardiol*. 2013;62:S32–S40.
9. Tsantis S, Kagadis GC, Katsanos K, Karnabatidis D, Bourantas G, Nikiforidis GC. Automatic vessel lumen segmentation and stent strut detection in intravascular optical coherence tomography. *Med Phys*. 2012;39:503–513.
10. Wang Z, Jenkins MW, Linderman GC, et al. 3-d stent detection in intravascular oct using a bayesian network and graph search. *IEEE Trans Med Imaging*. 2015;34:1549–1561.
11. Tenekecioglu E, Albuquerque FN, Sotomi Y, et al. Intracoronary optical coherence tomography: clinical and research applications and intravascular imaging software overview. *Catheter Cardiovasc Interv*. 2017;89:679–689.
12. Mintz GS, Pichard AD, Satler LF, Popma JJ, Kent KM, Leon MB. Three-dimensional intravascular ultrasonography: reconstruction of endovascular stents in vitro and in vivo. *J Clin Ultrasound*. 1993;21:609–615.
13. von Birgelen C, Mintz GS, Nicosia A, et al. Electrocardiogram-gated intravascular ultrasound image acquisition after coronary stent deployment facilitates on-line three-dimensional reconstruction and automated lumen quantification. *J Am Coll Cardiol*. 1997;30:436–443.
14. Umemoto T, Pacchioni A, Nikas D, Reimers B. Recent developments of imaging modalities of carotid artery stenting. *J Cardiovasc Surg*. 2017;58:25–34.
15. Kaple RK, Tsujita K, Maehara A, Mintz GS. Accuracy of stent measurements using ecg-gated greyscale intravascular ultrasound images: a validation study. *Ultrasound Med Biol*. 2009;35:1265–1270.
16. Gogas BD, Farooq V, Onuma Y, Serruys PW. The absorb bioresorbable vascular scaffold: an evolution or revolution in interventional cardiology? *Hellenic J Cardiol*. 2012;53:301–309.
17. Onuma Y, Serruys PW. Bioresorbable scaffold: the advent of a new era in percutaneous coronary and peripheral revascularization?. *Circulation*. 2011;123:779–797.
18. Canero C, Pujol O, Radeva P, et al. Optimal stent implantation: three-dimensional evaluation of the mutual position of stent and vessel via intracoronary echocardiography. In: *Computers in Cardiology*. Hannover, Germany: IEEE; 1999:261–264.
19. Dijkstra J, Koning G, Tuinenburg J. Automatic border detection in intravascular iltrasound images for quantitative measurements of the vessel, lumen and stent parameters. *Computers in Cardiology 2001.Vol. 28 (Cat. No.01CH37287)*, Vol. 1230. Berlin, Heidelberg: Springer; 2001:25–28.
20. Dijkstra J, Koning G, Tuinenburg JC, Oemrawsingh PV, von Birgelen C, Reiber JHC. (2002) Automatic stent border detection in IntraVascular UltraSound images for quantitative measurements of the stent parameters. In: Lemke HU, Inamura K, Doi K, Vannier MW, Farman AG, Reiber JHC (eds), *CARS 2002 Computer Assisted Radiology and Surgery*, Berlin: Springer.
21. Rotger D, Radeva P, Bruining N. Automatic detection of bioabsorbable coronary stents in ivus images using a cascade of classifiers. *IEEE Trans Inf Technol Biomed*. 2010;14:535–537.
22. Hua R, Pujol O, Ciompi F, et al. Stent strut detection by classifying a wide set of ivus features. In: *MICCAI Workshop on Computer Assisted Stenting*; 2012:130–137.
23. Gatta C, Balocco S, Ciompi F, Hemetsberger R, Rodriguez-Leor O, Radeva P. Real-time gating of ivus sequences based on motion blur analysis: method and quantitative validation. In: *MICCAI 2010, LNCS 6362/2010*; 2010:59–67 .
24. Balocco S, Ciompi F, Rigla J, Carrillo X, Mauri J, Radeva P. Intra-coronary stent localization in intravascular ultrasound sequences, a preliminary study. In: *MICCAI conference*, Vol. 10552. Québec City, Canada: Springer. 2017:10552.
25. Balocco S, Gatta C, Ciompi F, et al. Combining growcut and temporal correlation for ivus lumen segmentation. In: *IbPRIA, LNCS 6669/2011*; 2011:556–563.
26. Ciompi F, Pujol O, Gatta C, et al. Holimab: a holistic approach for media-adventitia border detection in intravascular ultrasound. *Med Image Anal*. 2012;16:1085–1100.
27. Lin J, Keogh E, Wei L, Lonardi S. Experiencing sax: a novel symbolic representation of time series. *Data Min Knowl Disc*. 2007;15:107.
28. Lee S-Y, Hong M-K. Stent evaluation with optical coherence tomography. *Yonsei Med J*. 2013;54:1075–1083.